Enhance Multi-View Classification through Multi-Scale Alignment and Expanded Boundary

Anonymous authors
Paper under double-blind review

Abstract

Multi-view classification aims at unifying the data from multiple views to complementarily enhance the classification performance. Unfortunately, two major problems in multi-view data are damaging model performance. The first is **feature heterogeneity**, which makes it hard to fuse features from different views. Considering this, we introduce a multi-scale alignment module, including an instance-scale alignment module and a prototype-scale alignment module to mine the commonality from an inter-view perspective and an inter-class perspective respectively, jointly alleviating feature heterogeneity. The second is **information redundancy** which easily incurs ambiguous data to blur class boundaries and impair model generalization. Therefore, we propose a novel expanded boundary by extending the original class boundary with fuzzy set theory, which adaptively adjusts the boundary to fit ambiguous data. By integrating the expanded boundary into the prototype-scale alignment module, our model further tightens the produced representations and reduces boundary ambiguity. Additionally, compared with the original class boundary, the expanded boundary preserves more margins for classifying unseen data, which guarantees the model generalization. Extensive experiment results across various datasets demonstrate the superiority of the proposed model against existing state-of-the-art methods.

1 Introduction

Multi-view data are widely applied in real-world applications by combining diverse heterogeneous features to describe the same object (Wang et al. (2023a); Zhang et al. (2024b)). Unluckily, **feature heterogeneity** and **information redundancy** concealed in the multi-view data have become the obstacles in multi-view learning (MVL) (Tan et al. (2024)). The feature heterogeneity means that the multi-view data are collected from different data distributions without a unified data format, causing fusion difficulty among the view features (Wang et al. (2024a)). The information redundancy signifies the latency of unnecessary features or ambiguous data, which hinders the ability to delimit the decision boundaries appropriately and naturally engenders classification ambiguity.

Existing MVL models mainly delve into alleviating the heterogeneity by finding informative common subspaces (Zhang et al. (2023a)) or ideal view weights (Hu et al. (2022)). The former explores the feature consistency and complementarity among the multi-view data (Lyu et al. (2024); Wang et al. (2024c)), which neglects significant class differences for separating reliable decision boundaries. The latter presumes that the qualities or importances of views are stable for samples (Kumar & Maji (2023)), and aims at allocating appropriate weights to different views (Houfar et al. (2023); Liu et al. (2023)). However, the varied view qualities fail to match diverse samples practically (Han et al. (2022b)), which also leads to unreliable decision boundaries. For instance, tigers and zebras have similar stripes but different colors, which makes the model give the color view a higher weight. Nevertheless, zebras and pandas have the same colors but disparate stripes, which induces the model to weigh more for the stripe view. Such scenarios easily result in unstable qualities or significances of different views to construct unreliable decision boundaries eventually.

Recent MVL works are dedicated to realizing trusted decisions by estimating the inherent uncertainties among multi-view data (Xu et al. (2023b; 2024)), and integrating multiple views at an evidence level. Actually, though they modify the logits to realize better classification decisions (Sensoy et al. (2018)), they still fail to deal with the aforementioned problems. To illustrate the

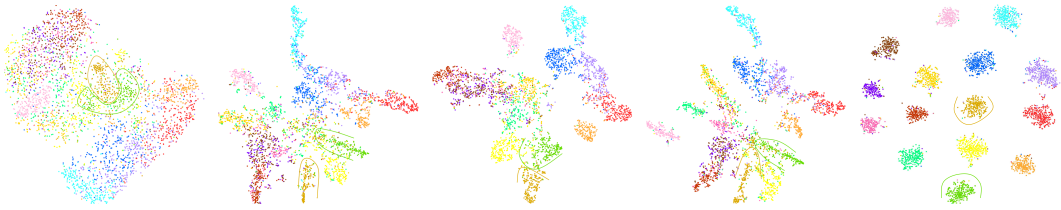

(a) Raw data (b) ETMC (c) PDMF (d) RCML (e) Ours

Figure 1: t-SNE on Scene15 dataset. The boundaries of the green class and the brown class are delineated. Compared with existing advanced models, our model shows much more distinct boundaries.

issue and our motivation intuitively, we provide the t-SNE in Figure 1, which includes our model MAMC (enhance multi-view classification through multi-scale alignment and expanded boundary) and three advanced MVL models ETMC (Han et al. (2022b)), PDMF (Xu et al. (2023b)), and RCML (Xu et al. (2024)) on Scene15 dataset. The t-SNE reflects two issues of current MVL models: 1) They cannot well mine the commonality to tighten the representations; 2) They ignore to exploit the class difference for clearing the ambiguous decision boundaries. These observations imply that ***they are unable to reduce the feature heterogeneity and the information redundancy satisfactorily***. Motivated by these observations, *our model focuses on* ***mining commonalities*** *among view representations and* ***learning clear decision boundaries*** *in the representation space simultaneously to tackle the feature heterogeneity and the information redundancy.* On the one hand, MAMC introduces a multi-scale alignment module to learn expressive view representations by mining the commonalities among views and class differences among prototypes; on the other hand, it expands the original class boundaries to the wider decision boundaries in the representation space, fitting ambiguous samples to clear the blurry areas between different classes adaptively. Specifically, the multi-scale alignment module includes two complementary contents: 1) An instance-scale alignment module mines the inter-view commonality by aligning the view representations of each instance. 2) A prototype-scale alignment module exploits the inter-class difference from the instances with the same labels to find appropriate decision boundaries jointly.

The design of expanded boundaries is based on fuzzy set theory (Zhang et al. (2023b)), and its expansion process involves fuzzy representations and crisp representations, where the fuzzy representations are defined in the fuzzy representation space while the crisp representations are in the normal representation space. The core of boundary expansion is based on the assumption that crisp representations are a special type of fuzzy representations. It enables us to find learnable positives of the crisp representations in the fuzzy representation space, which are then employed to construct elements of the expanded boundary. Finally, the expanded decision boundary is integrated into the prototype-scale alignment process. By narrowing the expanded boundary and its corresponding class prototype while distancing other class prototypes, the inter-class difference is sufficiently exploited. Additionally, the expanded boundary reserves extra space for instances that belong to the class latently, which is beneficial for improving the model generalization. Our contributions are summarized as follows:

- We propose MAMC to address the problems caused by the feature heterogeneity and the information redundancy. Through introducing the multi-scale alignment module, MAMC sufficiently mines the inter-view commonality to tighten instances and inter-class difference to delimit the decision boundaries.
- We propose a novel self-adaptive expanded boundary to tackle the ambiguous decision boundaries. By integrating the expanded boundary into the prototype-scale alignment module, the inter-class difference is reinforced to clear the ambiguous decision boundaries, while the representations inside the boundary are tightened.
- We explain the rationality of the model design theoretically, and extensive experimental results across diverse public datasets and comprehensive experimental analysis have verified that the proposed model shows significant superiority against the existing state-of-the-art models.

2 Preliminaries

2.1 Fuzzy Set Theory

Fuzzy set theory builds on classical (crisp) set theory by introducing the concept of membership degrees, which allows for fine-grained definitions of whether an element belongs to a set (Zadeh (1965)). A fuzzy set $\mathcal{A}$ in the universe $\mathbb{U}$ is characterized by a membership function $f_{\mathcal{A}}(x)$ which allocates each element in $\mathbb{U}$ with a real number in $[0,\ 1]$, where $\mathbb{U}$ is defined as a set that contains all the elements under consideration for a particular discussion or problem, and $f_{\mathcal{A}}(x)$ represents the membership degree of x in $\mathcal{A}$ (Zhelezniak et al. (2019)). Fuzzy set theory provides a powerful framework for reasoning about sets with uncertainty, but the specification of membership functions depends greatly on domain knowledge. Specifically, we have the following definitions:

Definition: A function $f_{\mathcal{A}}: \mathbb{U} \to \mathbb{L} \subseteq \mathbb{R}$ is called a membership function.

Definition: A tuple $\mathcal{A} = (\mathbb{U},\ \ f_{\mathcal{A}})$ including a universe $\mathbb{U}$ and a membership function $f_{\mathcal{A}}$ is called a fuzzy set.

Following the definitions, when $\mathbb{L} = [0,\ 1]$, $\mathcal{A}$ is a fuzzy set. When the membership function takes on only two values 0 and 1, namely $\mathbb{L} = \{0,\ 1\}$ according to whether x belongs to $\mathcal{A}$. In this case, $\mathcal{A}$ reduces to a classical set.

2.2 Multi-view Learning

Joint learning on multi-view data has been proven effective on various tasks, such as clustering (Zhuge et al. (2020); Shen et al. (2024a)), and classification (Jiang et al. (2024)). Current works are roughly divided into the subspace-based (Shen et al. (2024b)) and view-weighted approaches (Zhang et al. (2024a)). The first category aims at finding a common subspace where the consensus representations are generated for all the views Wang et al. (2023b). Canonical correlation analysis (CCA) based approaches are one type of representative methods that project different views into a subspace by maximally correlating them. (Kumar & Maji (2023)) proposed D2CCA that integrates the CCA theory with the objective function to find the joint representations. (Yuan et al. (2022)) proposed a canonical $\mathcal{F}$-correlation framework where each feature was projected into a certain space by an arbitrary nonlinear mapping. Meanwhile, many works are dedicated to searching optimal weights for different views. (Xu et al. (2020)) proposed to make deep interactive information using view-specific information in an adaptive weighted manner, and seamlessly integrated the view-specific information with a multi-view loss fusion strategy to achieve joint decisions. (Houfar et al. (2023)) attended the distinctions between different views because of the sample importances, and proposed a dynamic learning strategy for automatically weighting views and samples. However, the subspace-based approaches mainly focus on mining feature commonality to handle feature heterogeneity but ignore the inter-class difference for delimiting the decision boundaries. And the view-weighted approaches have trouble producing generalized weights for views, which also makes it hard to find an effective boundary. In summary, these approaches fail to tackle the problem caused by information redundancy, especially when ambiguous samples are distributed around the decision boundaries. Motivated by this, we focus on mining commonalities among view representations and learning clear decision boundaries in the representation space simultaneously to alleviate the feature heterogeneity and the information redundancy.

2.3 Multi-view Classification

Existing multi-view classification methods can generally be divided into two categories: feature fusion-based and decision-based methods. Feature fusion-based methods focus on effectively combining features from all views. MV-HFMD (Black & Souvenir (2024)) explores feature fusion by introducing a novel fusion scheme and mutual distillation to adapt neural networks for multi-view classification. Mmdynamics (Han et al. (2022a)) dynamically assesses the informativeness of both feature-level and view-level data across different samples, ensuring trustworthy integration of multiple views. However, these methods often neglect feature heterogeneity, which undermines the effectiveness of feature fusion. For the decision-based methods, they are dedicated to making more reasonable decisions. ETMC (Han et al. (2022b)) introduces a new paradigm for multi-view learning by dynamically integrating different views at the evidence level, thereby enhancing classification

reliability. RCML (Xu et al. (2024)) attends to that conflictive information in different views, and proposes a conflictive opinion aggregation strategy that exactly models the relation of multi-view common and view-specific reliabilities. MVAKNN (Fan et al. (2023)) utilizes the Dempster–Shafer theory to integrate information from each view, successfully extending adaptive KNN to a multi-view setting. IPMVSC (Hu et al. (2023)) constructs a multi-view fuzzy classification model inherited from the natural interpretability of fuzzy rule-based systems to realize interpretable classification. Many methods of this kind interact with the multiple views only in the decision phase, which cannot well integrate the information from all the views. In contrast, our model aligns view features during the representation learning phase and combines them in the decision phase, allowing for more effective and interactive information integration across all views.

3 Proposed Method

The proposed model aims to mine commonality and learn adaptive boundaries to deal with the problems caused by feature heterogeneity and information redundancy. The architecture of our model is shown in Figure 2, including view-specific representation extractors, a multi-scale alignment module, and a joint classifier. To detail the model architecture conveniently, we first provide some notations.

Notations. Formally, a multi-view dataset $\mathcal{D} = \{(\{\boldsymbol{x}_i^{(v)}\}_{v=1}^V, y_i) | 1 \leq i \leq N\}$ is defined as N $i.i.d.$ instances with V views and corresponding labels. We use a real-value vector $\boldsymbol{x}_i^{(v)} \in \mathbb{R}^{D_v}$ $(1 \leq v \leq V,\ i = 1, \cdots, N)$ to denote the feature vector of i-th instance for the v-th view, where D_v is the feature dimension of the v-th view and K is the number of classes. For the labels, we use a natural number $y_i \in \mathbb{N}$ to represent the ground truth of i-th instance and $\hat{\boldsymbol{y}}_i \in \{0,\ 1\}^K$ to represent the corresponding one-hot vector. To integrate information from the multiple views, our model aims at learning a desired mapping $f : \mathcal{X} \to \mathcal{Y}$ from the multi-view dataset $\mathcal{D}$ for better predicting the correct label of unseen instances.

3.1 View-Specific Representation Learning

Heterogeneous multi-view data conceal many inherent issues, such as inconsistent dimensions of view features. To address the issues, we employ multiple view-specific auto-encoders to generate exclusive view representations in the same dimension (Zhong et al. (2024)). For the v-th view data $\boldsymbol{X}^{(v)}$, we apply a view-specific encoder $E^{(v)}$ to produce the view representation matrix $\boldsymbol{H}^{(v)}$ and a decoder $D^{(v)}$ to restore the raw view feature, where the encoder and the decoder are constructed by multi-layer perceptions (MLPs). The reconstruction process is given by

$$\mathcal{L}_{rec} = \frac{1}{V} \sum_{v=1}^{V} \left\| \boldsymbol{X}^{(v)} - D^{(v)} \left(E^{(v)}(\boldsymbol{X}^{(v)}) \right) \right\|_F^2 . \tag{1}$$

3.2 Instance-Scale Alignment

The key to reducing the feature heterogeneity of multi-view data is to mine the inter-view commonality. Contrastive learning exploits commonality among data by pulling together the positives while pushing away the negatives (Wang et al. (2024b)). The instance-scale alignment module combines contrastive learning and regards all the view representations of each instance as positives while others as negatives. Concretely, the view representations $\{\boldsymbol{h}_i^{(v)}\}_{v=1}^V$ abstracted from the view-specific encoders are recognized as positives and others are negatives. Hence, the instance-scale alignment loss is

$$\mathcal{L}_{ins} = -\frac{1}{NV} \sum_{v=1}^{V} \sum_{u \neq v} \sum_{i=1}^{N} \log \frac{e^{-Dis\left(\boldsymbol{h}_i^{(v)}, \boldsymbol{h}_i^{(u)}\right) \cdot \tau_{ins}}}{e^{-Dis\left(\boldsymbol{h}_i^{(v)}, \boldsymbol{h}_i^{(u)}\right) \cdot \tau_{ins}} + \sum_{r=u,v} \sum_{j \neq i} e^{-Dis\left(\boldsymbol{h}_i^{(v)}, \boldsymbol{h}_j^{(r)}\right) \cdot \tau_{ins}}}, \tag{2}$$

where τ_{ins} is a temperature coefficient, and $Dis\,(\cdot, \cdot)$ is a distance function. By aligning the positive view representations, the critical common semantics to recognize similar samples are exploited, while the feature heterogeneity is mitigated. By differing the negatives, the discrepancies between different samples gradually emerge, thereby making the learned representations more suitable for delimiting the decision boundaries.

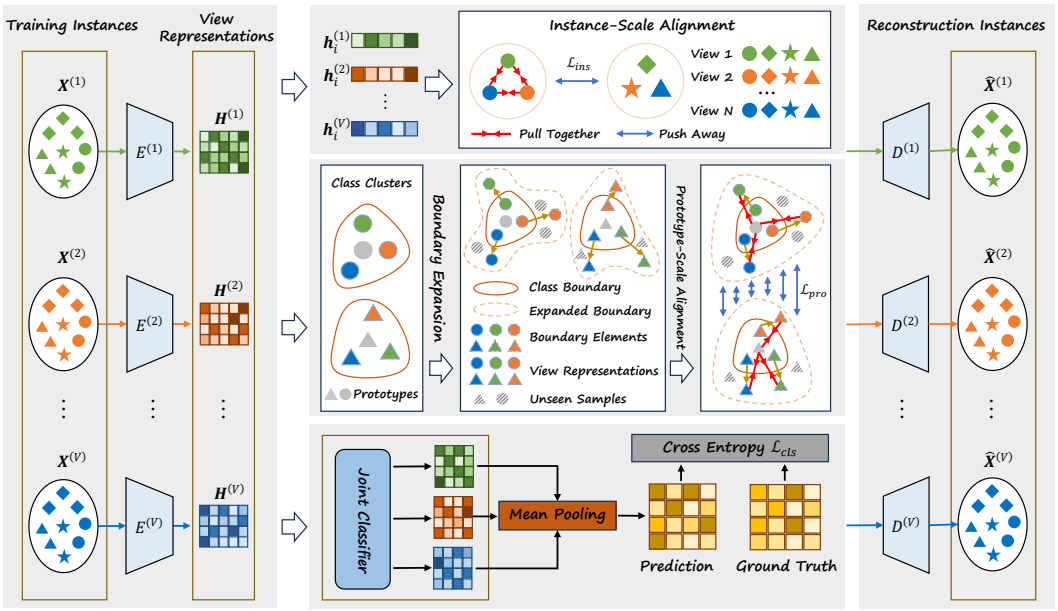

Figure 2: Three main components of the proposed model: (1) View-specific representation extractors. Multiple view-specific auto-encoders abstract critical view representations $\{\boldsymbol{H}^{(v)}\}_{v=1}^{V}$ from multi-view data $\{\boldsymbol{X}^{(v)}\}_{v=1}^{V}$. (2) Multi-scale alignment module. The instance-scale alignment module aligns view representations $\{\boldsymbol{h}_i^{(v)}\}_{v=1}^{V}$ of each instance $\boldsymbol{x}_i$, where the icons with various shapes correspond to different instances and those with different colors correspond to representations from different views. The prototype-scale alignment module integrates the adaptive expanded boundaries, and then aligns the view representations with the same labels. (3) Joint classifier. All the view representations are sent into the joint classifier to obtain fused predictions.

3.3 Prototype-Scale Alignment

In contrast to the instance-scale alignment module, the goal of the prototype-scale alignment module is to exploit the inter-class difference for delimiting clear decision boundaries. The core of achieving this goal is to construct the expanded boundary.

3.3.1 Expanded Boundary

Since the information redundancy in multi-view data easily blurs the decision boundaries, general prototype learning ignoring the inter-class difference has limited ability to work effectively. Instead, we propose an adaptive expanded boundary to assist the prototype-scale alignment module, expecting to clear the ambiguous boundaries.

To sufficiently gather the class information for exploiting the inter-class difference, we collect all the view representations with the same labels to construct the class prototypes and use them to centralize the view representations. For the training data of the k-th class, the centralizing process is defined as:

$$\boldsymbol{c}_k = \frac{1}{V\,|Y_k|} \sum_{v=1}^{V} \sum_{y_i=k} \boldsymbol{h}_i^{(v)}, \tag{3}$$

$$\boldsymbol{z}_i^{(v)} = \boldsymbol{h}_i^{(v)} - \boldsymbol{c}_k,\ v = 1, \cdots, V, \tag{4}$$

where $\boldsymbol{z}_i^{(v)}$ is the centralized representation vector of the i-th instance in the v-th view, Y_k is the set including the training data whose labels are k, and $|\cdot|$ is used for counting the cardinality of a set. $\boldsymbol{c}_k$ is the prototype vector of the k-th class, which filters the high-frequency noise by averaging.

A key step of boundary expansion is to construct the fuzzy representation space with membership functions, and the Gaussian membership function is the most universal one (Li et al. (2023)). The

appropriate number of membership functions imparts the expanded boundary with more adaptability. To this end, we adopt L Gaussian membership functions. For the l-th membership function, the corresponding membership degree is defined by

$$\boldsymbol{r}_{i,j,l}^{(v)} = \exp\left\{-\frac{\left(\boldsymbol{z}_{i,j}^{(v)} - \boldsymbol{m}_{j,l}\right)^2}{2\boldsymbol{\delta}_{j,l}^2}\right\},\ l = 1, 2, \cdots, L,\ j = 1, 2, \cdots, d, \tag{5}$$

where d is the dimension of the view representation, $\boldsymbol{z}_{i,j}^{(v)}$ is the j-th element of i-th instance in the v-th centralized view representation vector, $\boldsymbol{m}_{j,l}$ and $\boldsymbol{\delta}_{j,l}$ are the trainable mean and standard deviation of the l-th Gaussian membership function respectively. These membership degrees are fused to obtain the final one for producing fuzzy representations, and the process is defined as

$$\tilde{\boldsymbol{r}}_{i,j}^{(v)} = Comb\left\{\boldsymbol{r}_{i,j,l}^{(v)}\right\},\ l = 1, 2, \cdots, L, \tag{6}$$

$$\widetilde{\boldsymbol{Z}}^{(v)} = \widetilde{\boldsymbol{R}}^{(v)} \odot \boldsymbol{Z}^{(v)}, \tag{7}$$

where $\tilde{\boldsymbol{r}}_{i,j}^{(v)}$ is the element of the membership degree matrix $\widetilde{\boldsymbol{R}}^{(v)}$, and $\odot$ is Hadamard product to transform the crisp view representation $\boldsymbol{Z}^{(v)}$ into the fuzzy representation $\widetilde{\boldsymbol{Z}}^{(v)}$. $Comb$ is the combination operator to fuse membership degrees and how to determine it will be explained later.

According to properties of membership functions, each value of $\widetilde{\boldsymbol{R}}^{(v)}$ is limited in [0, 1], which implies that the crisp representations can be viewed as one special case of fuzzy ones. Based on this, we regard crisp representations and fuzzy representations as positives. Besides, we assume that their discrepancies reflected by the coordinate differences are tolerable since the discrepancies between positives do not significantly violate the commonality semantics in general. Inspired by this, we implement the tolerable discrepancy to expand the original class boundary, and the boundary expansion process is depicted in Figure 3. Mathematically, the elements of the expanded boundary are transformed by the coordinates of the fuzzy representations, which are formalized as

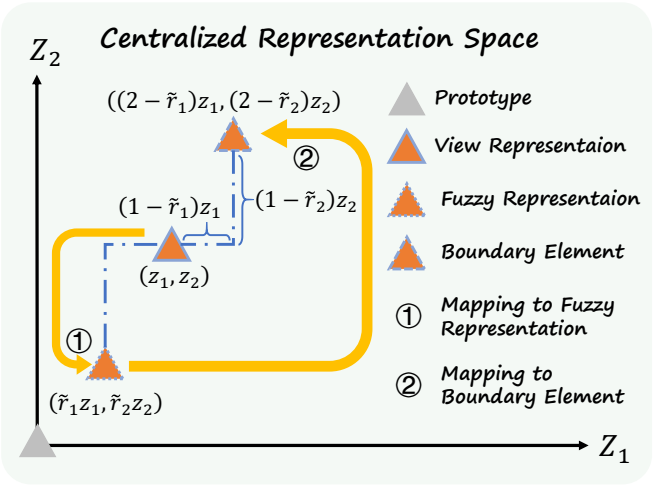

Figure 3: The boundary expansion process in 2-dimension space. One centralized view representation ▲ is firstly utilized to calculate the fuzzy representation ▲, and then mapped as the boundary element ▲.

$$\overline{\boldsymbol{Z}}^{(v)} = \widetilde{\boldsymbol{Z}}^{(v)} + 2\left(\mathbf{1} - \widetilde{\boldsymbol{R}}^{(v)}\right) \odot \boldsymbol{Z}^{(v)} = \left(\mathbf{2} - \widetilde{\boldsymbol{R}}^{(v)}\right) \odot \boldsymbol{Z}^{(v)}, \tag{8}$$

where $\overline{\boldsymbol{Z}}^{(v)}$ is composed of boundary elements, $\mathbf{1}$ and $\mathbf{2}$ are two real value matrices whose each element is 1 and 2 respectively. Though simple, the expanded boundary inherits two desired properties from the fuzzy representations: 1) **Semantics-positive**. The boundary elements are supposed to be the positives of crisp representations, which benefit recognizing the ambiguous samples far away from the class centers. 2) **Self-adaptive**. The expanded boundaries are based on the learnable membership functions and could adjust adaptively to involve the ambiguous samples in the training process. These two properties aim to capture nearly all the samples inside each boundary for fully exploiting the inter-class difference.

3.3.2 Loss Function

After expanding the original boundaries, we restore the coordinates of the centralized fuzzy representation matrix $\overline{\boldsymbol{Z}}$ by adding their corresponding class prototype $\boldsymbol{C}$ as the restored fuzzy representation matrix $\overline{\boldsymbol{H}}$, since it is tough to separate the classes in a centralized representation space whose class centers are all origin points. The expansion of the original class boundaries leads to the new-born prototype of boundary elements $\widetilde{\boldsymbol{C}}$, which causes a trade-off between $\boldsymbol{C}$ and $\widetilde{\boldsymbol{C}}$. We mix up both to harvest the fused prototype $\overline{\boldsymbol{C}}$ by a linear combination as

$$\overline{\boldsymbol{C}} = \eta \boldsymbol{C} + (1-\eta)\,\widetilde{\boldsymbol{C}}, \tag{9}$$

where each prototype vector of $\boldsymbol{C}$ is calculated by Eq. (3), $\widetilde{\boldsymbol{C}}$ is calculated by averaging the boundary elements of each class, and η is a balance coefficient to reconcile $\boldsymbol{C}$ and $\widetilde{\boldsymbol{C}}$.

To generalize for unseen data as much as possible, we expect to maximize the spectrum of each class, which is equal to maximizing the variance within each class. Meanwhile, we expect to achieve better separateness among different classes and compactness within each class, which intends to maximize the distances between different classes while minimizing the variance within each class. Considering these factors, the loss function is formalized as a *minimax game* by

$$\mathcal{L}_{pro} = \min_{\mathcal{P}+\mathcal{V}} \max_{\mathcal{V}} (\mathcal{P}+\mathcal{V}), \tag{10}$$

where $\mathcal{P}$ is defined to distance different classes and $\mathcal{V}$ to tighten samples within each class while generalizing for unseen data. They could be defined as

$$\begin{cases} \mathcal{P} = -\frac{1}{NKV}\sum_{v=1}^{V}\sum_{k=1}^{K}\sum_{n=1}^{N}\left\|\overline{\boldsymbol{h}}_n^{(v)} - \overline{\boldsymbol{c}}_k\right\|_2^2 \\ \mathcal{V} = \frac{1}{NV}\sum_{v=1}^{V}\sum_{k=1}^{K}\sum_{y_i=k}\left\|\overline{\boldsymbol{h}}_i^{(v)} - \overline{\boldsymbol{c}}_k\right\|_2^2 \end{cases}. \tag{11}$$

For convenience, we let $\mathcal{Q} = \mathcal{P} + \mathcal{V}$, and propose an upper bound of $\mathcal{Q}$ in our model, expecting to further optimize $\mathcal{Q}$ by optimizing its upper bound. We define the upper bound $\mathcal{Q}_{pro}$ as

$$\mathcal{Q}_{pro} = -\frac{1}{NV}\sum_{v=1}^{V}\sum_{k=1}^{K}\sum_{y_i=k}\log\frac{e^{-\tau_{pro}\left\|\overline{\boldsymbol{h}}_i^{(v)}-\overline{\boldsymbol{c}}_k\right\|_2^2}}{\sum_j e^{-\tau_{pro}\left\|\overline{\boldsymbol{h}}_i^{(v)}-\overline{\boldsymbol{c}}_j\right\|_2^2}}, \tag{12}$$

where $\overline{\boldsymbol{c}}_k$ is the fused prototype vector of the k-th class, $\overline{\boldsymbol{h}}_i^{(v)}$ is the restored boundary elements of the i-th instance in the v-th view, and τ_{pro} is the temperature coefficient to control the compactness of classes. Generally, higher τ_{pro} makes the classes more compact. We provide the theoretical proof that $\mathcal{Q}_{pro}$ is an upper bound of $\mathcal{Q}$ in the Appendix.

In the prototype-scale alignment loss, we integrate all the view representations to serve as the class samples since partial view information easily releases misleading information or loses critical information, which may lead to ambiguous decision boundaries. In this way, all the view information is gathered to collaboratively form the inter-class difference for delimiting the decision boundaries. Additionally, according to (Oord et al. (2018)), contrastive learning evaluates the mutual information between the raw view data and the restored boundary elements, namely

$$I\left(\boldsymbol{x}_i, \left\{\overline{\boldsymbol{h}}_i^{(v)}\right\}_{v=1}^{V}\right) \geq \log\left(\mathcal{N}\right) - \mathcal{Q}_{pro}, \tag{13}$$

where $I\left(\cdot\right)$ is used to calculate the mutual information, $\mathcal{N}$ is the sample amount participated in the loss function. This inequation reveals that more negatives raise the lower bound and preserve more complete information from the raw data for better alignment performance. Typically, integrating all the view representations is a flexible way to multiply the amount of negatives.

3.3.3 Combination Operator Determination

The combination operator $Comb$ in Eq. (6) is crucial to the expanded boundaries. On the one hand, the $Comb$ operator cannot damage the self-adaptive ability of the expanded boundaries.

On the other hand, the $Comb$ operator controls the class variances to generalize for unseen data. The former is achieved by the learnable membership functions, and the latter is affected by the determination of the $Comb$.

Theorem 1. When employing $Min\ Pooling$ as the $Comb$ operator, the overall variance of each class is maximized. The proof is provided in the Appendix.

Therefore, when the ideal $Comb$ operator is defined as the minimal of the membership functions, the spectrum of each class is maximized. It means that the expanded boundary could generalize more latent (unseen) samples belonging to corresponding classes. Finally, the prototype-scale alignment loss $\mathcal{L}_{pro}$ in Eq. (10) is reduced as

$$\mathcal{L}_{pro} = \min -\frac{1}{NV}\sum_{v=1}^{V}\sum_{i=1}^{N}\log\frac{e^{-\tau_{pro}\left\|\overline{\boldsymbol{h}}_i^{(v)}-\overline{\boldsymbol{c}}_i\right\|_2^2}}{\sum_j e^{-\tau_{pro}\left\|\overline{\boldsymbol{h}}_i^{(v)}-\overline{\boldsymbol{c}}_j\right\|_2^2}}. \tag{14}$$

3.4 Classification Prediction

During the classification process, we employ a joint classifier that adopts the parameter sharing strategy, and it has several merits: 1) Shared parameters receive information from all the views simultaneously, which is conducive to constructing a classifier specific for the multi-view data. 2) The multi-scale alignment module has mined the inter-view commonality and the inter-class difference to construct clear decision boundaries, reducing the demand on the complex classifier with a large number of parameters. The model prediction is produced by averaging the outputs of the joint classifier by

$$\hat{\boldsymbol{p}}_i = \frac{1}{V}\sum_{v=1}^{V}\boldsymbol{p}_i^{(v)} = \frac{1}{V}\sum_{v=1}^{V} g\left(\boldsymbol{h}_i^{(v)}\right), \tag{15}$$

where $g(\cdot)$ is a logistic classifier, $\boldsymbol{p}_i^{(v)}$ is the output of $g(\cdot)$ in the v-th view, and $\hat{\boldsymbol{p}}_i$ is the final prediction. During training, we use the cross-entropy to calculate the classification loss as

$$\mathcal{L}_{cls} = -\frac{1}{N}\sum_{i=1}^{N}\sum_{j=1}^{K}\hat{\boldsymbol{y}}_{ij}\log\hat{\boldsymbol{p}}_{ij}. \tag{16}$$

where $\hat{\boldsymbol{p}}_i$ is the final prediction from Eq. (15), and $\hat{\boldsymbol{p}}_{ij}$ is its j-th element. $\hat{\boldsymbol{y}}_i$ refers to the one-hot vector label of the i-th instance, and $\hat{\boldsymbol{y}}_{ij}$ is the corresponding element in this vector. The overall loss $\mathcal{L}_{all}$ comprises four parts, namely reconstruction loss, classification loss, instance-scale alignment loss, and prototype-scale alignment loss, which is given by

$$\mathcal{L}_{all} = \mathcal{L}_{rec} + \mathcal{L}_{cls} + \alpha\mathcal{L}_{ins} + \beta\mathcal{L}_{pro}, \tag{17}$$

where α and β are penalty coefficients. $\mathcal{L}_{all}$ focuses on mining the commonality among different views and clearing ambiguity areas around the decision boundaries, which successfully alleviates the damage of the feature heterogeneity and the information redundancy.

4 Experiments

In our experiment, we evaluate our model on eight public multi-view datasets including HandWritten, Scence15, PIE, CCV, Animal, 100Leaves, Hdigit, and YoutubeFace. To show the effectiveness of the proposed model, five state-of-the-art methods are adopted to compare with, including **mm-dynamics** (Han et al. (2022a)), **ETMC** (Han et al. (2022b)), **UMDL** (Xu et al. (2023a)), **PDMF** (Xu et al. (2023b)), **IPMVSC** (Hu et al. (2023)), **MV-HFMD** (Black & Souvenir (2024)), and **RCML** (Xu et al. (2024)). For each dataset, we split 80% instances for training and the remainder for testing. To obtain reliable results, we implement the same dataset split ten times for all the models. More details of the datasets are provided in the Appendix.

4.1 Experimental Results

Table 1 presents the classification results between our model and other baseline models, and we adopt Accuracy (Acc), Purity, Recall, and Macro-F1 as the metrics. From the statistical comparisons, some important observations are revealed:

Table 1: Classification results (%) with baseline models. The best results are highlighted in bold. "OOM" indicates that the models raise the out-of-memory failure.

Datasets	Metrics	mmdynamics	ETMC	UMDL	PDMF	IPMVSC	MV-HFMD	RCML	Ours
HandWritten	Acc	98.5±0.5	96.8±0.7	97.7±0.5	98.2±0.7	98.7±0.4	98.2±0.6	97.1±0.9	**98.9±0.4**
	Precision	98.5±0.5	96.8±0.7	97.8±0.5	98.3±0.7	98.7±0.4	98.2±0.5	97.1±0.9	**98.9±0.4**
	Recall	98.5±0.5	96.9±0.7	97.7±0.5	98.3±0.7	98.7±0.4	98.2±0.6	97.2±0.9	**98.9±0.4**
	Macro F1	98.5±0.5	96.8±0.7	97.7±0.5	98.2±0.7	98.7±0.4	98.1±0.5	97.1±0.9	**98.9±0.4**
Scene15	Acc	62.0±2.2	66.5±1.8	63.3±0.4	67.8±1.1	71.8±1.4	80.7±1.2	70.0±1.0	**81.5±0.7**
	Precision	57.3±2.8	66.6±2.5	61.2±0.7	65.8±2.8	73.8±0.7	80.6±1.6	70.6±1.3	**81.0±0.6**
	Recall	60.1±2.2	65.3±1.6	62.7±0.5	65.9±1.1	70.5±0.8	80.3±1.3	68.9±1.3	**80.8±0.7**
	Macro F1	57.6±2.5	62.8±1.8	61.1±0.7	63.0±1.4	69.1±0.9	80.0±1.4	67.1±1.1	**80.5±0.7**
PIE	Acc	72.5±3.7	90.5±2.3	71.1±3.3	88.7±3.0	91.9±2.0	86.8±2.4	91.8±2.9	**93.1±1.7**
	Precision	70.6±4.0	88.0±3.8	74.6±3.9	87.6±3.8	81.7±2.1	87.7±2.7	91.1±3.4	**92.8±2.1**
	Recall	70.6±3.7	89.6±3.6	71.1±3.3	87.3±4.9	82.1±1.8	88.9±2.4	91.0±3.5	**93.6±1.8**
	Macro F1	67.4±3.8	87.4±3.8	69.3±3.5	85.7±4.5	80.5±2.5	83.8±6.1	89.8±3.9	**92.1±2.0**
CCV	Acc	29.6±1.1	42.6±1.4	36.2±1.5	50.5±1.4	42.6±1.8	53.4±0.9	42.4±1.7	**54.0±1.1**
	Precision	22.8±2.8	41.4±2.6	35.5±1.3	48.5±1.3	48.3±2.0	51.1±1.1	42.3±2.2	**53.0±1.3**
	Recall	23.2±1.0	37.1±1.4	33.7±1.4	45.4±1.3	35.5±1.3	50.5±0.8	37.0±1.4	**50.6±1.0**
	Macro F1	20.1±1.1	36.0±1.6	33.1±1.4	45.1±1.5	34.3±1.5	50.4±0.9	35.9±1.5	**51.0±0.9**
Animal	Acc	56.7±1.4	56.6±0.8	34.0±1.1	57.0±0.7	39.5±1.9	59.6±0.7	56.8±1.2	**60.2±1.1**
	Precision	52.4±2.2	53.3±3.2	33.7±0.9	49.5±0.6	37.3±3.9	56.5±0.6	54.5±2.5	**56.7±1.3**
	Recall	49.9±1.3	49.7±1.0	30.4±0.8	47.2±0.7	33.3±2.5	53.7±0.4	49.5±1.2	**53.8±0.8**
	Macro F1	50.4±1.4	49.7±1.1	30.4±0.7	46.7±0.6	33.3±2.7	54.0±0.5	49.6±1.3	**54.1±0.8**
100Leaves	Acc	93.5±1.5	90.8±2.1	98.4±0.8	97.7±0.7	66.1±4.1	98.3±0.2	88.6±1.5	**98.5±1.1**
	Precision	93.6±1.2	90.5±2.5	**98.7±0.8**	97.7±0.9	70.2±3.4	98.4±0.0	88.7±2.0	98.5±1.0
	Recall	93.9±1.1	91.3±2.4	98.4±0.9	98.0±1.0	69.0±2.0	98.9±0.2	89.4±1.4	**99.0±0.7**
	Macro F1	92.7±1.3	89.3±2.7	98.3±0.9	97.5±1.0	64.0±2.7	98.4±0.1	87.0±1.7	**98.5±1.0**
Hdigit	Acc	99.6±0.1	90.8±2.1	98.0±0.2	99.4±0.2	97.8±0.3	84.1±2.0	98.3±0.3	**99.8±0.1**
	Precision	99.6±0.1	98.4±0.2	98.0±0.2	99.4±0.2	97.8±0.3	88.9±1.7	98.3±0.3	**99.8±0.1**
	Recall	99.6±0.1	98.4±0.2	98.0±0.2	99.4±0.2	97.9±0.3	87.5±2.0	98.3±0.3	**99.8±0.1**
	Macro F1	99.6±0.1	98.4±0.2	98.0±0.2	99.4±0.2	97.8±0.3	86.5±2.3	98.3±0.3	**99.8±0.1**
YoutubeFace	Acc	56.3±0.3	71.9±2.1	OOM	85.6±0.3	28.2±0.3	83.4±0.8	52.6±1.0	**87.1±0.2**
	Precision	74.8±0.6	83.2±0.8	OOM	89.2±0.4	29.9±4.0	85.6±1.0	83.1±1.0	**89.5±0.4**
	Recall	46.0±0.3	67.7±3.1	OOM	84.3±0.4	5.4±0.3	82.8±0.8	38.7±1.3	**86.2±0.3**
	Macro F1	53.5±0.5	73.0±2.8	OOM	86.6±0.3	5.2±0.4	83.9±0.8	46.6±1.4	**87.7±0.1**

1) The proposed model shows extraordinary superiority among the comparing methods across all the datasets, especially on the Scene15 dataset. Compared with existing methods, our model is ideal to align all the view information while learning satisfactory decision boundaries, which are critical for the classification task.
2) For datasets that all the models receive wonderful results such as HandWritten, 100Leaves, and Hdigit datasets, the satisfactory decision boundaries are easily delimited. However, the proposed model could further improve the performance, which implies the rooted ambiguity near the decision boundaries is further alleviated.
3) MV-HFMD shows a very outstanding performance, which implies the significance of effective feature fusion in multi-view learning. However, it may neglect to address the feature heterogeneity that plays an important role in facilitating the feature fusion, so the model performance is somewhat limited when compared with our model.
4) Compared with a fuzzy multi-view learning model IPMVSC that focuses on using fuzzy rules to realize an interpretable classifier, our model attends to the feature-level issues and applies the fuzzy set theory in the representation space. Besides, from the results, we find that IPMVSC does not work well on large datasets, but our model works well on both small and large datasets.

In summary, the proposed model successfully mines the commonality to tackle the feature heterogeneity, learns the adaptive boundaries to mitigate the harm from the information redundancy, and preserves margins for unseen data to enhance the model generalization.

4.2 Ablation Study

To evaluate the effectiveness of the multi-scale alignment module and the rationality of the $Comb$ operator determination, we conduct the ablation study whose results are provided in Table 2, and have the following observations:
1) According to the results, the instance-scale alignment and the prototype-scale alignment work effectively to improve the inter-view commonalities and inter-class differences, which are essential

Table 2: Results of ablation study on classification (%), which are concerned with the functions of the multi-scale alignment module and the selection of $Comb$ operator.

$\mathcal{L}_{cls}$	$\mathcal{L}_{rec}$	$\mathcal{L}_{ins}$	$\mathcal{L}_{pro}$	$Comb$	HandWritten	Animal	PIE	CCV
✓	✓				96.08±0.47	55.78±0.04	84.93±0.36	42.48±0.58
✓	✓	✓			97.44±0.54	56.95±0.42	89.71±1.20	49.34±3.33
✓	✓		✓		96.76±0.68	56.95±0.65	90.81±0.82	51.01±2.39
✓	✓	✓	✓		97.46±1.10	57.80±0.15	91.54±0.82	51.69±2.18
✓	✓		✓	Min	98.15±0.41	59.20±0.75	92.40±0.92	52.34±0.34
✓	✓	✓	✓	Min	**98.85±0.42**	**60.16±1.03**	**93.11±1.72**	**53.97±1.14**
✓	✓	✓	✓	Max	97.67±0.42	58.26±0.31	91.92±0.60	52.18±2.68
✓	✓	✓	✓	Mean	98.69±0.30	59.74±0.81	92.46±1.09	53.11±0.40

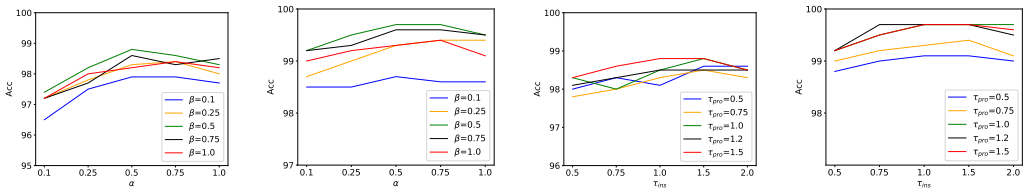

(a) HandWritten (b) Hdigit (c) HandWritten (d) Hdigit

Figure 4: Hyperparameter analysis on the HandWritten and Hdigit datasets. (a) and (b) delve into the functions of penalty coefficients α and β, (c) and (d) delve into the functions of temperature coefficients τ_{ins} and τ_{pro}.

for addressing the problems caused by feature heterogeneity and information redundancy.
2) In contrast to the instance-scale alignment, the prototype-scale alignment shows greater improvements, which is attributed to exploiting the helpful inter-class differences for delimiting the clear boundaries.
3) Compared with different $Comb$ operators, the $Min\ Pooling$ exhibits the best performance, which demonstrates the superiority of preserving more margins for classifying unseen data.

4.3 Hyperparameter Analysis

We conduct the hyperparameter analysis on two penalty coefficients α and β, and two temperature coefficients τ_{ins} and τ_{pro}. For α and β, we vary their values from $\{0.1, 0.25, 0.5, 0.75, 1\}$, and for τ_{ins} and τ_{pro}, we vary their values from $\{0.5, 0.75, 1.0, 1.5, 2.0\}$ and $\{0.5, 0.75, 1.0, 1.2, 1.5\}$ respectively. The results on HandWritten dataset and Hdigit dataset are presented in Figure 4. Compared with the temperature coefficients, the penalty coefficients affect the results more significantly, which illustrates the effectiveness of the multi-scale alignment module. Besides, the best results are prone to larger temperature coefficients that weigh more on similar samples.

4.4 Further Analysis

Due to the page limit, we provide further analysis in the Appendix, including the t-sne visualization, convergence analysis, and the demonstration of the model to learn clear decision boundaries.

5 Conclusion

Feature heterogeneity and information redundancy among the multi-view data are likely to cause the difficulty of feature fusion and the ambiguity around the decision boundaries, which motivates us to propose a novel MVL model MAMC for addressing the problems. MAMC employs the view-specific auto-encoders to abstract exclusive view representations and introduces a multi-scale alignment module to reduce the feature heterogeneity by mining the feature commonality. Besides, we propose a novel expanded boundary to exploit the class difference, which benefits to clear the ambiguity from the information redundancy. Extensive experiments demonstrate the superior performance and rational design of the proposed model.

References

Samuel Black and Richard Souvenir. Multi-view classification using hybrid fusion and mutual distillation. In *Proceedings of the IEEE/CVF Winter Conference on Applications of Computer Vision*, pp. 270–280, 2024.

Zizhu Fan, Yijing Huang, Chao Xi, and Qiang Liu. Multi-view adaptive k-nearest neighbor classification. *IEEE Transactions on Artificial Intelligence*, 5(3):1221–1234, 2023.

Zongbo Han, Fan Yang, Junzhou Huang, Changqing Zhang, and Jianhua Yao. Multimodal dynamics: Dynamical fusion for trustworthy multimodal classification. In *Proceedings of the IEEE/CVF Conference on Computer Vision and Pattern Recognition*, pp. 20707–20717, 2022a.

Zongbo Han, Changqing Zhang, Huazhu Fu, and Joey Tianyi Zhou. Trusted multi-view classification with dynamic evidential fusion. *IEEE Transactions on Pattern Analysis and Machine Intelligence*, 45(2):2551–2566, 2022b.

Khamis Houfar, Djamel Samai, Fadi Dornaika, Azeddine Benlamoudi, Khaled Bensid, and Abdelmalik Taleb-Ahmed. Automatically weighted binary multi-view clustering via deep initialization (aw-bmvc). *Pattern Recognition*, 137:109281, 2023.

Shizhe Hu, Ruilin Geng, Zhaoxu Cheng, Chaoyang Zhang, Guoliang Zou, Zhengzheng Lou, and Yangdong Ye. A parameter-free multi-view information bottleneck clustering method by cross-view weighting. In *Proceedings of the 30th ACM International Conference on Multimedia*, pp. 3792–3800, 2022.

Xingchen Hu, Xinwang Liu, Witold Pedrycz, Qing Liao, Yinghua Shen, Yan Li, and Siwei Wang. Multi-view fuzzy classification with subspace clustering and information granules. *IEEE Transactions on Knowledge and Data Engineering*, 35(11):11642–11655, 2023.

Zhangqi Jiang, Tingjin Luo, and Xinyan Liang. Deep incomplete multi-view learning network with insufficient label information. In *Proceedings of the AAAI Conference on Artificial Intelligence*, pp. 12919–12927, 2024.

Debamita Kumar and Pradipta Maji. Discriminative deep canonical correlation analysis for multi-view data. *IEEE Transactions on Neural Networks and Learning Systems*, pp. 1–13, 2023.

Andong Li, Zhaohong Deng, Wei Zhang, Zhiyong Xiao, Kup-Sze Choi, Yueying Liu, Shudong Hu, and Shitong Wang. Multiview transfer representation learning with tsk fuzzy system for eeg epilepsy detection. *IEEE Transactions on Fuzzy Systems*, 32(1):38–52, 2023.

Chengliang Liu, Jie Wen, Xiaoling Luo, and Yong Xu. Incomplete multi-view multi-label learning via label-guided masked view-and category-aware transformers. In *Proceedings of the AAAI Conference on Artificial Intelligence*, pp. 8816–8824, 2023.

Gengyu Lyu, Zhen Yang, Xiang Deng, and Songhe Feng. L-vsm: Label-driven view-specific fusion for multiview multilabel classification. *IEEE Transactions on Neural Networks and Learning Systems*, pp. 1–15, 2024.

Aaron van den Oord, Yazhe Li, and Oriol Vinyals. Representation learning with contrastive predictive coding. *arXiv preprint arXiv:1807.03748*, pp. 1–13, 2018.

Murat Sensoy, Lance Kaplan, and Melih Kandemir. Evidential deep learning to quantify classification uncertainty. *Advances in neural information processing systems*, pp. 1–11, 2018.

Qiangqiang Shen, Yongyong Chen, Changqing Zhang, Yonghong Tian, and Yongsheng Liang. Pick-and-place transform learning for fast multi-view clustering. *IEEE Transactions on Image Processing*, 33:1272–1284, 2024a.

Qiangqiang Shen, Tingting Xu, Yongsheng Liang, Yongyong Chen, and Zhenyu He. Robust tensor recovery for incomplete multi-view clustering. *IEEE Transactions on Multimedia*, 26:3856–3870, 2024b.

Xin Tan, Ce Zhao, Chengliang Liu, Jie Wen, and Zhanyan Tang. A two-stage information extraction network for incomplete multi-view multi-label classification. In *Proceedings of the AAAI Conference on Artificial Intelligence*, pp. 15249–15257, 2024.

Bing Wang, Ximing Li, Changchun Li, Shengsheng Wang, and Wanfu Gao. Escaping the neutralization effect of modality features fusion in multimodal fake news detection. *Information Fusion*, pp. 102500, 2024a.

Jiaan Wang, Jianfeng Qu, Kexin Wang, Zhixu Li, Wen Hua, Ximing Li, and An Liu. Improving the robustness of knowledge-grounded dialogue via contrastive learning. In *Proceedings of the AAAI Conference on Artificial Intelligence*, pp. 19135–19143, 2024b.

Jing Wang, Songhe Feng, Gengyu Lyu, and Zhibin Gu. Triple-granularity contrastive learning for deep multi-view subspace clustering. In *Proceedings of the 31st ACM International Conference on Multimedia*, pp. 2994–3002, 2023a.

Jing Wang, Songhe Feng, Gengyu Lyu, and Jiazheng Yuan. Surer: Structure-adaptive unified graph neural network for multi-view clustering. In *Proceedings of the AAAI Conference on Artificial Intelligence*, pp. 15520–15527, 2024c.

Shiye Wang, Changsheng Li, Yanming Li, Ye Yuan, and Guoren Wang. Self-supervised information bottleneck for deep multi-view subspace clustering. *IEEE Transactions on Image Processing*, 32: 1555–1567, 2023b.

Cai Xu, Zehui Li, Ziyu Guan, Wei Zhao, Xiangyu Song, Yue Wu, and Jianxin Li. Unbalanced multi-view deep learning. In *Proceedings of the 31st ACM International Conference on Multimedia*, pp. 3051–3059, 2023a.

Cai Xu, Wei Zhao, Jinglong Zhao, Ziyu Guan, Yaming Yang, Long Chen, and Xiangyu Song. Progressive deep multi-view comprehensive representation learning. In *Proceedings of the AAAI Conference on Artificial Intelligence*, pp. 10557–10565, 2023b.

Cai Xu, Jiajun Si, Ziyu Guan, Wei Zhao, Yue Wu, and Xiyue Gao. Reliable conflictive multi-view learning. In *Proceedings of the AAAI Conference on Artificial Intelligence*, pp. 16129–16137, 2024.

Jinglin Xu, Wenbin Li, Xinwang Liu, Dingwen Zhang, Ji Liu, and Junwei Han. Deep embedded complementary and interactive information for multi-view classification. In *Proceedings of the AAAI Conference on Artificial Intelligence*, pp. 6494–6501, 2020.

Yun-Hao Yuan, Jin Li, Yun Li, Jipeng Qiang, Yi Zhu, Xiaobo Shen, and Jianping Gou. Learning canonical f-correlation projection for compact multiview representation. In *Proceedings of the IEEE/CVF Conference on Computer Vision and Pattern Recognition*, pp. 19260–19269, 2022.

Lotfi A Zadeh. Fuzzy sets. *Information and Control*, 8(3):338–353, 1965.

Chaoyang Zhang, Zhengzheng Lou, Qinglei Zhou, and Shizhe Hu. Multi-view clustering via triplex information maximization. *IEEE Transactions on Image Processing*, 32:4299–4313, 2023a.

Chenglong Zhang, Yang Fang, Xinyan Liang, Xingyu Wu, Bingbing Jiang, et al. Efficient multi-view unsupervised feature selection with adaptive structure learning and inference. In *Proceedings of the Thirty-Third International Joint Conference on Artificial Intelligence*, pp. 5443–5452, 2024a.

Chenglong Zhang, Xinyan Liang, Peng Zhou, Zhaolong Ling, Yingwei Zhang, Xingyu Wu, Weiguo Sheng, and Bingbing Jiang. Scalable multi-view unsupervised feature selection with structure learning and fusion. In *Proceedings of the 32nd ACM International Conference on Multimedia*, pp. 1–9, 2024b.

Wei Zhang, Zhaohong Deng, Te Zhang, Kup-Sze Choi, and Shitong Wang. One-step multiview fuzzy clustering with collaborative learning between common and specific hidden space information. *IEEE Transactions on Neural Networks and Learning Systems*, pp. 1–14, 2023b.

Vitalii Zhelezniak, Aleksandar Savkov, April Shen, Francesco Moramarco, Jack Flann, and Nils Y Hammerla. Don't settle for average, go for the max: Fuzzy sets and max-pooled word vectors. In *International Conference on Learning Representations*, pp. 1–17, 2019.

Qiyu Zhong, Gengyu Lyu, and Zhen Yang. Align while fusion: A generalized nonaligned multiview multilabel classification method. *IEEE Transactions on Neural Networks and Learning Systems*, pp. 1–10, 2024.

Wenzhang Zhuge, Hong Tao, Tingjin Luo, Ling-Li Zeng, Chenping Hou, and Dongyun Yi. Joint representation learning and clustering: A framework for grouping partial multiview data. *IEEE Transactions on Knowledge and Data Engineering*, 34(8):3826–3840, 2020.

A Additional Proofs

A.1 Proof of Proposition 1

Proposition 1: $\mathcal{Q}_{pro}$ is an upper bound of $\mathcal{Q}$.

Proof: Without losing generalization, we let $\tau_{pro} = 1$, and we have

$$
\begin{aligned}
\mathcal{Q}_{pro} &= -\frac{1}{NV}\sum_{v=1}^{V}\sum_{k=1}^{K}\sum_{y_i=k}\log\frac{e^{-\tau_{pro}\left\|\overline{\boldsymbol{h}}_i^{(v)}-\overline{\boldsymbol{c}}_k\right\|_2^2}}{\sum_j e^{-\tau_{pro}\left\|\overline{\boldsymbol{h}}_i^{(v)}-\overline{\boldsymbol{c}}_j\right\|_2^2}} \\
&= \frac{1}{NV}\sum_{v=1}^{V}\sum_{k=1}^{K}\sum_{y_i=k}\log\frac{\sum_j e^{-\left\|\overline{\boldsymbol{h}}_i^{(v)}-\overline{\boldsymbol{c}}_j\right\|_2^2}}{e^{-\left\|\overline{\boldsymbol{h}}_i^{(v)}-\overline{\boldsymbol{c}}_k\right\|_2^2}} \\
&= \frac{1}{NV}\sum_{v=1}^{V}\sum_{k=1}^{K}\sum_{y_i=k}\left(\log\sum_j e^{-\left\|\overline{\boldsymbol{h}}_i^{(v)}-\overline{\boldsymbol{c}}_j\right\|_2^2} - \log e^{-\left\|\overline{\boldsymbol{h}}_i^{(v)}-\overline{\boldsymbol{c}}_k\right\|_2^2}\right) \\
&= \frac{1}{NV}\sum_{v=1}^{V}\sum_{k=1}^{K}\sum_{v_i=k}\left(\log\sum_j e^{-\left\|\overline{\boldsymbol{h}}_i^{(v)}-\overline{\boldsymbol{c}}_j\right\|_2^2} + \left\|\overline{\boldsymbol{h}}_i^{(v)}-\overline{\boldsymbol{c}}_k\right\|_2^2\right) \\
&\approx \frac{1}{NV}\sum_{v=1}^{V}\sum_{k=1}^{K}\sum_{y_i=k}\left(\log K\mathbb{E}\left[e^{-\left\|\overline{\boldsymbol{h}}_i^{(v)}-\overline{\boldsymbol{c}}_j\right\|_2^2}\right] + \left\|\overline{\boldsymbol{h}}_i^{(v)}-\overline{\boldsymbol{c}}_k\right\|_2^2\right) \\
&= \frac{1}{NV}\sum_{v=1}^{V}\sum_{k=1}^{K}\sum_{y_i=k}\left(\log\mathbb{E}\left[e^{-\left\|\overline{\boldsymbol{h}}_i^{(v)}-\overline{\boldsymbol{c}}_j\right\|_2^2}\right] + \left\|\overline{\boldsymbol{h}}_i^{(v)}-\overline{\boldsymbol{c}}_k\right\|_2^2 + \log K\right).
\end{aligned}
\tag{18}
$$

K is a constant to denote the number of classes, and we ignore it to obtain a new loss $\mathcal{Q}'_{pro}$, namely

$$
\mathcal{Q}'_{pro} = \frac{1}{NV}\sum_{v=1}^{V}\sum_{k=1}^{K}\sum_{y_i=k}\left(\log\mathbb{E}\left[e^{-\left\|\overline{\boldsymbol{h}}_i^{(v)}-\overline{\boldsymbol{c}}_j\right\|_2^2}\right] + \left\|\overline{\boldsymbol{h}}_i^{(v)}-\overline{\boldsymbol{c}}_k\right\|_2^2\right). \tag{19}
$$

According to the *Jensen's inequality*, we could get

$$
\exp\left\{\mathbb{E}\left[-\left\|\overline{\boldsymbol{h}}_i^{(v)}-\overline{\boldsymbol{c}}_j\right\|_2^2\right]\right\} \leq \mathbb{E}\left[\exp\left\{-\left\|\overline{\boldsymbol{h}}_i^{(v)}-\overline{\boldsymbol{c}}_j\right\|_2^2\right\}\right]. \tag{20}
$$

Considering that the logarithmic function is a monotonically increasing function, we have

$$
\mathcal{Q}'_{pro} \geq \frac{1}{NV}\sum_{v=1}^{V}\sum_{k=1}^{K}\sum_{y_i=k}\left(\mathbb{E}\left[-\left\|\overline{\boldsymbol{h}}_i^{(v)}-\overline{\boldsymbol{c}}_j\right\|_2^2\right] + \left\|\overline{\boldsymbol{h}}_i^{(v)}-\overline{\boldsymbol{c}}_k\right\|_2^2\right) \approx \mathcal{Q}. \tag{21}
$$

A.2 Proof of Theorem 1

Theorem 1. When employing $Min\ Pooling$ as the $Comb$ operator, the overall variance of each class is maximized.

Proof: Without losing generalization, we let $\tau_{pro} = 1$, and we have

$$\begin{aligned}
\mathcal{Q}_{pro} &= -\frac{1}{NV}\sum_{v=1}^{V}\sum_{k=1}^{K}\sum_{y_i=k}\log\frac{e^{-\left\|\overline{\boldsymbol{h}}_i^{(v)}-\overline{\boldsymbol{c}}_k\right\|_2^2}}{\sum_j e^{-\left\|\overline{\boldsymbol{h}}_i^{(v)}-\overline{\boldsymbol{c}}_j\right\|_2^2}} \\
&= \frac{1}{NV}\sum_{v=1}^{V}\sum_{k=1}^{K}\sum_{y_i=k}\left(\log\sum_j e^{-\left\|\overline{\boldsymbol{h}}_i^{(v)}-\overline{\boldsymbol{c}}_j\right\|_2^2}+\left\|\overline{\boldsymbol{h}}_i^{(v)}-\overline{\boldsymbol{c}}_k\right\|_2^2\right) \\
&= \frac{1}{NV}\sum_{v=1}^{V}\sum_{k=1}^{K}\sum_{y_i=k}\left(\log\sum_j e^{-\left\|\overline{\boldsymbol{h}}_i^{(v)}-\overline{\boldsymbol{c}}_j\right\|^2}\right)+\frac{1}{NV}\sum_{v=1}^{V}\sum_{k=1}^{K}\sum_{y_i=k}\left(\left\|\overline{\boldsymbol{h}}_i^{(v)}-\overline{\boldsymbol{c}}_k\right\|_2^2\right) \\
&\approx \frac{1}{NV}\sum_{v=1}^{V}\sum_{i=1}^{N}\left(\log\sum_j e^{-\left\|\overline{\boldsymbol{h}}_i^{(v)}-\overline{\boldsymbol{c}}_j\right\|_2^2}\right)+\sum_{k=1}^{K}Var(\overline{\boldsymbol{c}}_k),
\end{aligned} \tag{22}$$

where $Var\left(\bar{\boldsymbol{c}}_k\right)$ stands for the variance of the k-th class cluster. Actually, it could be observed that $\mathcal{V} = \frac{1}{NV}\sum_{v=1}^{V}\sum_{k=1}^{K}\sum_{y_i=k}\left\|\overline{\boldsymbol{h}}_i^{(v)}-\overline{\boldsymbol{c}}_k\right\|_2^2 = \sum_{k=1}^{K}Var(\overline{\boldsymbol{c}}_k)$. In practice, we weigh the crisp prototype more and set η to approximate 1, then we have

$$\lim_{\eta\to 1}\mathcal{V} = \lim_{\eta\to 1}\sum_{k=1}^{K}Var\left(\overline{\boldsymbol{c}}_k\right) = \sum_{k=1}^{K}Var\left(\boldsymbol{c}_k\right). \tag{23}$$

When applying the centralized representations for constructing the expanded boundary, the maximal overall variance within each class cluster is formalized as

$$\begin{aligned}
\max\lim_{\eta\to 1}\mathcal{V} &= \max\sum_{k=1}^{K}Var(\boldsymbol{c}_k) = \max\sum_{v=1}^{V}\sum_{k=1}^{K}\sum_{y_i=k}\left\|\overline{\boldsymbol{h}}_i^{(v)}-\boldsymbol{c}_k\right\|_2^2 \\
&= \max\sum_{v=1}^{V}\sum_{k=1}^{K}\sum_{y_i=k}\left\|\overline{\boldsymbol{z}}_i^{(v)}\right\|_2^2 = \max\sum_{v=1}^{V}\sum_{k=1}^{K}\sum_{y_i=k}\left\|\left(\mathbf{2}-\tilde{\boldsymbol{r}}_i^{(v)}\right)\odot\boldsymbol{z}_i^{(v)}\right\|_2^2 \\
&= \max\sum_{v=1}^{V}\sum_{i=1}^{N}\left\|\left(\mathbf{2}-\tilde{\boldsymbol{r}}_i^{(v)}\right)\odot\boldsymbol{z}_i^{(v)}\right\|_2^2,
\end{aligned} \tag{24}$$

where K is the number of classes. Obviously, for each representation, when each element of $\tilde{\boldsymbol{r}}_i^{(v)}$ becomes smaller, $\mathcal{V}$ becomes greater, which is in line with

$$\left\|\left(\mathbf{2}-\left\{\tilde{\boldsymbol{r}}_i^{(v)}\right\}_{min}\right)\odot\boldsymbol{z}_i^{(v)}\right\|_2^2 \geq \left\|\left(\mathbf{2}-\left\{\tilde{\boldsymbol{r}}_i^{(v)}\right\}_{other}\right)\odot\boldsymbol{z}_i^{(v)}\right\|_2^2, \tag{25}$$

where $\left\{\tilde{\boldsymbol{r}}_i^{(v)}\right\}_{min}$, and $\left\{\tilde{\boldsymbol{r}}_i^{(v)}\right\}_{other}$ are the membership degree vectors, which are the outputs of $Min\ Pooling$, and other simple $Comb$ operators such as $Mean\ Pooling$, or $Max\ Pooling$. Finally, we have

$$\sum_{v=1}^{V}\sum_{i=1}^{N}\left\|\left(\mathbf{2}-\left\{\tilde{\boldsymbol{r}}_i^{(v)}\right\}_{min}\right)\odot\boldsymbol{z}_i^{(v)}\right\|_2^2 \geq \sum_{v=1}^{V}\sum_{i=1}^{N}\left\|\left(\mathbf{2}-\left\{\tilde{\boldsymbol{r}}_i^{(v)}\right\}_{other}\right)\odot\boldsymbol{z}_i^{(v)}\right\|_2^2. \tag{26}$$

This means that among the simple $Comb$ operators, $Min\ Pooling$ as the $Comb$ could maximize the overall variance of each class.

B Experiment Settings

B.1 Datasets

We provide the complete statistics of the used datasets in Table 3. HandWritten [1] and Hdigit [2] datasets are composed of handwritten digit images, PIE [3] and YoutubeFace [4] datasets collect the data on facial recognition and expression recognition, Scene15 [5] dataset contains images from 15 different scene categories, CCV [6] dataset comprises videos under complex conditions, Animal [7] dataset contains images of different animals, 100Leaves [8] dataset is composed of images from 100 different leaves.

Table 3: Statistics of datasets, which include the number of instances, classes, and the view dimensions.

Dataset	Instances	Classes	Views	View dimensions
HandWritten	2,000	10	6	240/76/216/47/64/6
Scene15	4,485	15	3	20/59/40
PIE	680	68	3	484/256/279
CCV	6,773	20	3	20/20/20
Animal	11,673	20	4	2,689/2,000/2,001/2,000
100Leaves	1,600	100	3	60/60/60
Hdigit	10,000	10	2	784/256
YoutubeFace	101,499	31	5	64/64/512/647/838

B.2 Implementation Details

The proposed model is implemented in Pytorch and trained with an SGD optimizer. The dimension settings of the encoder and decoder are formed by $\{D_v,\ 1.4 \times 512,\ 1.2 \times 512,\ 512\}$ and $\{512,\ 0.6 \times D_v,\ 0.8 \times D_v,\ D_v\}$ respectively. The number of membership functions L is set as 5. The learning rate is chosen from $\left\{1e^{-3}, 3e^{-3}, 5e^{-3}, 1e^{-2}\right\}$, and the coefficients α and β are chosen from $\{0.1, 0.25, 0.5, 0.75, 1\}$. The temperature coefficients τ_{ins} and τ_{pro} are chosen from $\{0.5, 0.75, 1.0, 1.5, 2.0\}$ and $\{0.5, 0.75, 1.0, 1.2, 1.5\}$ respectively. All experiments are conducted on a server with 8 NVIDIA GeForce 3090 (24 GB memory each).

B.3 Training Algorithm

The proposed MAMC includes three main components of the proposed model, namely view-specific representation extractors, a multi-scale alignment module, and a joint classifier. Among the three components, the view-specific auto-encoders abstract critical view representations from multi-view data, and the multi-scale alignment module mines the inter-view commonality and inter-class difference. The joint classifier calculates the fused predictions. Algorithm 1 presents the detailed training process of the proposed MAMC.

C Supplementary Experiments

C.1 Learning Clear Decision Boundaries

Information redundancy in the multi-view data would lead to ambiguous boundaries. To further verify that MAMC has the ability to learn clear decision boundaries, we implement our model on

[1] HandWritten: http://archive.ics.uci.edu/ml/datasets/Multiple+Features.
[2] Hdigit: https://archive.ics.uci.edu/ml/index.php.
[3] PIE: https://www.cs.cmu.edu/afs/cs/project/PIE.
[4] YoutubeFace: https://www.cs.tau.ac.il/wolf/ytfaces.
[5] Scene15: http://www-cvr.ai.uiuc.edu/ponce_grp/data/scene15.
[6] CCV: http://www.ee.columbia.edu/ln/dvmm/CCV.
[7] Animal: https://www.cs.ucf.edu/ xmzhang/datasets.
[8] 100Leaves: https://archive.ics.uci.edu/ml/datasets/One-hundred+plant+species+leaves+data+set.

Algorithm 1 Training process of MAMC

Input: Multi-view dataset: $\mathcal{D} = \{(\{\boldsymbol{x}_i^{(v)}\}_{v=1}^{V}, y_i)|1 \leq i \leq N\}$; Hyperparameters τ_{ins}, τ_{pro}, α, and β; Training epochs T.
Output: Model parameters.
Initialization: Initialize the parameters of the neural network.
Process:

for $epoch = 1$ **to** T **do**
  Calculate the view representation matrices $\{\boldsymbol{H}^{(v)}\}_{v=1}^{V}$ with view-specific auto-encoders.
  \\ Instance-scale alignment
  Realize the instance-scale alignment by Eq. (2).
  \\ Prototype-scale alignment
  Centralize the view representations by Eq. (3)-(4).
  Calculate the boundary elements by Eq. (5)-(8).
  Realize the prototype-scale alignment by Eq. (14).
  \\ Classification prediction
  Calculate the classification loss by Eq. (15)-(16).
end for

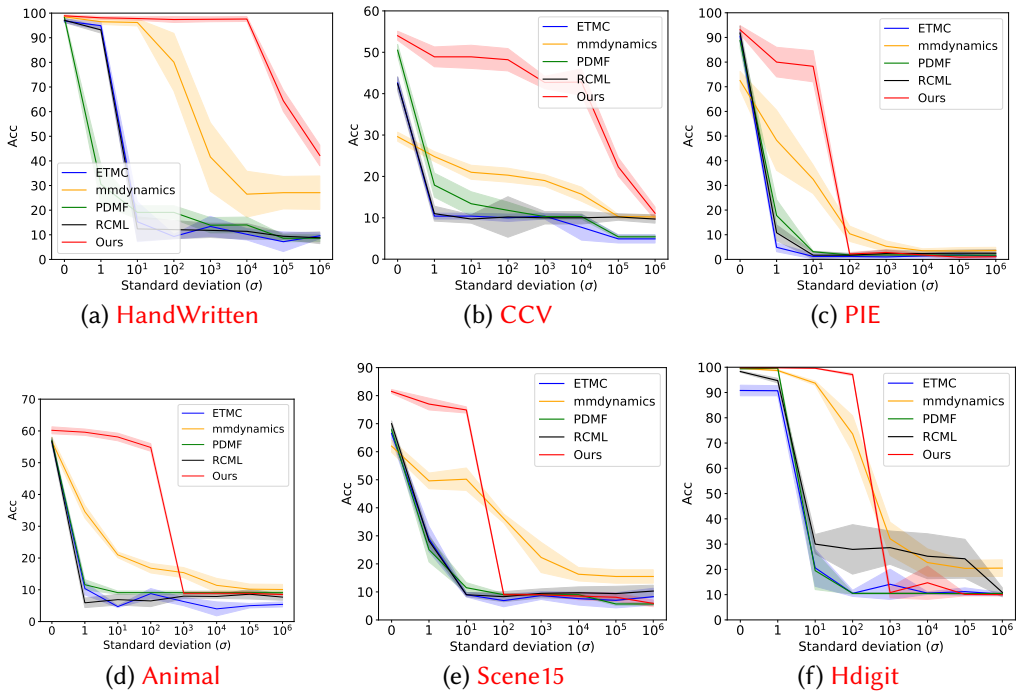

(a) HandWritten (b) CCV (c) PIE

(d) Animal (e) Scene15 (f) Hdigit

Figure 5: Performance comparison on multi-view datasets with different levels of noise.

manufactured ambiguous data. In our experiments, we add Gaussian noise with different levels of deviations σ to half of the views, and provide the comparison results in Figure 5. We discover that when the noise increases, the performance of all the models drops quickly since larger noise results in more ambiguous boundaries. Even so, the performance of our model descends more slowly than other models, especially when the noise is small. Actually, the data noise in the real multi-view data is not large, which demonstrates that MAMC exploits the desired inter-difference from all the view information to clear the ambiguous decision boundaries.

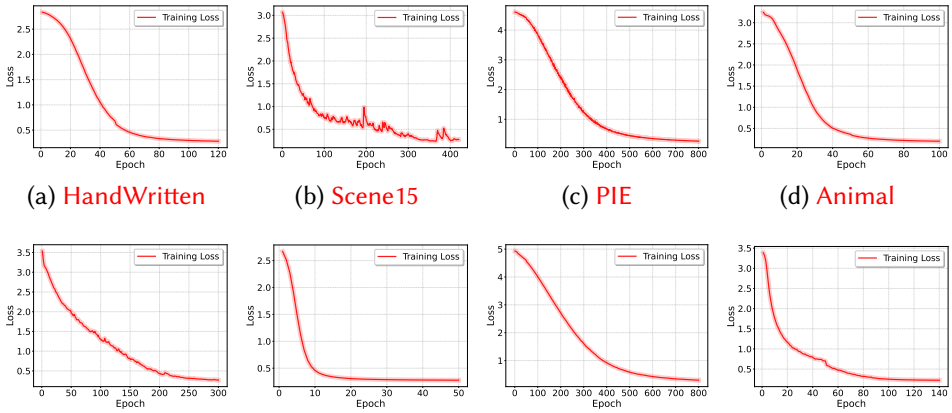

(a) HandWritten (b) Scene15 (c) PIE (d) Animal

(e) CCV (f) Hdigit (g) 100Leaves (h) YoutubeFace

Figure 6: The convergence analysis of MAMC across all the datasets.

C.2 Loss Analysis

We conduct the convergence analysis of the proposed method across all the datasets, where experimental results of loss values are illustrated in Figure 6. It is observed that the losses decrease steadily and converge between 50 and 800 epochs across all datasets. Such a phenomenon empirically confirms the convergence of MAMC.

C.3 Visualization

In this experiment, we provide the t-SNE of the comparative MVL models and raw data in Figure 7. In practice, one instance is encoded as several view representations, which are then concatenated as a final representation vector. The final representation vector is input into the t-SNE algorithm to obtain the visualization. From the results, we could find that though the raw data are ambiguous, most models disentangle different classes to some degree. However, our model shows much better results since it mines the feature commonalities to tighten samples inside each class and exploits inter-class differences for separating different classes.

C.4 Complexity Comparison

We present the model complexity comparison in Table 4 and Table 5. Table 4 lists the complexity of all the models, and we can find that our model has the same level of complexity as some comparative models. Table 5 provides detailed computational overhead analysis including MACs, concrete running time, and Parameters. For a fair comparison, we set the same batch size and training epochs for all the models. From all the statistics, we could find that our model is not cumbersome, but is competitive with some advanced models.

Table 4: Complexity comparison between the comparative models and the proposed model.

Model	Complexity
mmdynamics	$\mathcal{O}(N)$
ETMC	$\mathcal{O}(N)$
UMDL	$\mathcal{O}(N^3)$
PDMF	$\mathcal{O}(N^2)$
RCML	$\mathcal{O}(N)$
Ours	$\mathcal{O}(N^2)$

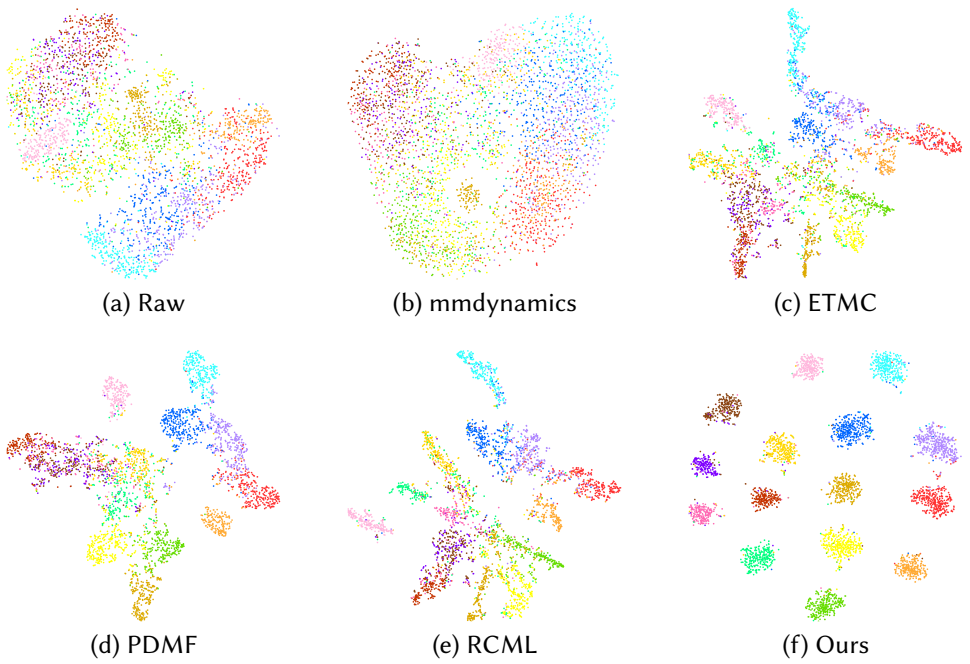

Figure 7: t-SNE of the comparative models and the proposed model on Scene15 dataset.

Table 5: Complexity comparison among the comparative models and the proposed model.

Datasets	Metrics	mmdynamics	ETMC	UMDL	PDMF	RCML	Ours
HandWritten	Running Time	21.911s	35.739s	10057.537s	21.972s	17.064s	23.302s
	MACs	267.871M	3.323M	1273.548M	189.989M	1.661M	1373.655M
	Parameters	1.0543M	0.0066M	5.2389M	1.722M	0.0066M	5.353M
Scene15	Running Time	28.996s	42.596s	31938.726s	45.678s	22.922s	41.651s
	MACs	66.604M	0.457M	132.890M	68.387M	0.457M	617.869M
	Parameters	0.264M	0.002M	20.632M	1.098M	0.002M	3.197M
PIE	Running Time	11.525s	11.233s	2721.368s	9.214s	7.775s	17.499s
	MACs	536.394M	17.739M	248.090M	188.088M	2.217M	996.040M
	Parameters	2.099M	0.070M	1.429M	1.540M	0.070M	4.622M
CCV	Running Time	40.678s	61.986s	29783.373s	69.529s	37.905s	65.490s
	MACs	56.521M	0.307M	125.338M	9.978M	0.307M	263.633M
	Parameters	0.225M	0.001M	46.361M	1.331M	0.001M	3.323M
Animal	Running Time	650.847s	181.911s	52103.473s	221.021s	119.074s	177.946s
	MACs	7643.710M	44.493M	1269.197M	576.355M	44.493M	9360.186M
	Parameters	29.873M	0.174M	141.214M	10.937M	0.174M	37.353M
100Leaves	Running Time	12.697s	16.173s	7386.190s	19.825s	10.078s	44.393s
	MACs	247.370M	4.915M	142.234M	80.740M	4.915M	672.518M
	Parameters	0.971M	0.020M	3.113M	0.814M	0.020M	3.323M
Hdigit	Running Time	57.370s	58.236s	44589.832s	85.163s	41.918s	59.256s
	MACs	506.520M	0.666M	211.558M	42.877M	2.662M	883.593M
	Parameters	1.982M	0.010M	100.825M	2.614M	0.010M	4.245M
YoutubeFace	Running Time	1660.614s	598.449s	—	513.350s	523.801s	702.112s
	MACs	4393.923M	67.456M	—	1466.827M	67.456M	7988.087M
	Parameters	4.328M	0.066M	—	15.840M	0.066M	8.544M